



### Science Arts & Métiers (SAM)

is an open access repository that collects the work of Arts et Métiers Institute of Technology researchers and makes it freely available over the web where possible.

This is an author-deposited version published in: <https://sam.ensam.eu>  
Handle ID: <http://hdl.handle.net/10985/24824>

#### To cite this version :

Maria-Rosa ARDIGO-BESNARD, Aurélien BESNARD, Yoann PINOT, Florian BUSSIÈRE, J.-P. CHATEAU-CORNU, C. VANDENABEELE, S. LUCAS, Noé WATIEZ, Armel DESCAMPS-MANDINE, Claudie JOSSE, Arnaud PROIETTI - Austenitic-to-austenitic-ferritic stainless steel transformation via PVD powder surface functionalization and spark plasma sintering - Materialia - Vol. 33, p.102002 - 2024

Any correspondence concerning this service should be sent to the repository

Administrator : [scienceouverte@ensam.eu](mailto:scienceouverte@ensam.eu)



# Austenitic-to-austenitic-ferritic stainless steel transformation via PVD powder surface functionalization and spark plasma sintering

M.R. Ardigo-Besnard<sup>a,\*</sup>, A. Besnard<sup>b</sup>, Y. Pinot<sup>b</sup>, F. Bussière<sup>a</sup>, J.-P. Chateau-Cornu<sup>a</sup>, C. Vandenaabeele<sup>c</sup>, S. Lucas<sup>c,d</sup>, N. Watiez<sup>b</sup>, A. Descamps-Mandine<sup>e</sup>, C. Josse<sup>e</sup>, A. Proietti<sup>e</sup>

<sup>a</sup> Laboratoire Interdisciplinaire Carnot de Bourgogne (ICB), UMR 6303 CNRS, Univ. Bourgogne, BP 47870, 21078 DIJON Cedex, France

<sup>b</sup> Arts et Metiers Institute of Technology, LaBoMaP, Univ. Bourgogne Franche-Comté, HESAM Université, 71250 Cluny, France

<sup>c</sup> Innovative Coating Solutions, 11 Place Saint Pierre, 5380 Forville, Belgium

<sup>d</sup> Laboratoire d'Analyse par Réactions Nucléaires (LARN), Namur Institute of Structured Matter (NISM), University of Namur, 61 Rue de Bruxelles, 5000 Namur, Belgium

<sup>e</sup> Centre de Microcaractérisation Raimond Castaing (CNRS UAR 3623), Espace Clement Ader, 3 rue Caroline Aigle, 31400 Toulouse, France

---

## A B S T R A C T

### Keywords:

PVD  
Coated powder  
Powder metallurgy  
Microstructure  
Alloy development

The present work investigates a new alloy design approach to elaborate stainless steel grades with an austenitic-ferritic microstructure. The originality of the study is the use, as starting material, of a 316 L austenitic powder coated by a thin chromium layer deposited by physical vapor deposition (PVD) technique. The coated powder was then consolidated by spark plasma sintering (SPS), a powder metallurgy process allowing the fast elaboration of dense materials with a fine-grained microstructure. The chromium coating, characterized by scanning and transmission electron microscopy, presents a columnar microstructure, formed by nanometric crystallites, well reproduced by the simulation of the film growth. The characterizations performed after sintering show that the initial austenitic powder particles are still visible in the bulk microstructure. On the other hand, a tetragonal  $\sigma$  phase enriched in chromium and molybdenum forms in the interparticular regions. After annealing treatment followed by quenching, the tetragonal phase transforms into the expected ferrite. The results prove that using a coated powder is a promising and innovative way to elaborate new steel grades with a two-phase austenitic-ferritic microstructure. This original approach can have the advantage of obtaining steels with a controlled microstructure and the desired amount of phases in the final bulk.

## 1. Introduction

Stainless steels containing both austenite and ferrite are known to have higher mechanical properties (ductility and strength) and better corrosion resistance than the mono-phase austenitic and ferritic ones [1–4]. For these reasons, austenitic-ferritic stainless steels are typically used in critical environments, such as in the chemical, petrochemical, oil, and nuclear industries [5,6]. On the other hand, this kind of steel is quite difficult to machine, mainly due to its high tensile strength, fracture toughness, work hardening rate, and low thermal conductivity [7]. During the last years, the elaboration of austenitic-ferritic stainless steels by additive manufacturing (AM) developed extensively, due to the possibility to obtain near-net-shape parts, with complex and different geometries, limiting post-process machining. Moreover, AM processes allow the elaboration of materials with very fine microstructures,

resulting from rapid cooling rates [3,8–11]. However, post-process treatments are almost systematically necessary for the following reasons:

- to obtain a good balance between austenitic and ferritic microstructure [3,12];
- to eliminate internal defects, such as porosity [13,14];
- to dissolve intermetallic phases, such as  $\sigma$ - and  $\chi$ -phases, which are known to precipitate in austenitic-ferritic stainless steels when exposed to high temperatures (between 650 and 1000 °C) [5,15–17] and considerably affect the mechanical and corrosion properties.

Köhler et al. [18] mixed an austenitic AISI 316 L powder with different fractions of duplex stainless steel AISI 318LN powder prior to the laser powder bed fusion (LPBF) process, to elaborate a material with

---

\* Corresponding author.

E-mail address: [maria-rosa.ardigo-besnard@u-bourgogne.fr](mailto:maria-rosa.ardigo-besnard@u-bourgogne.fr) (M.R. Ardigo-Besnard).



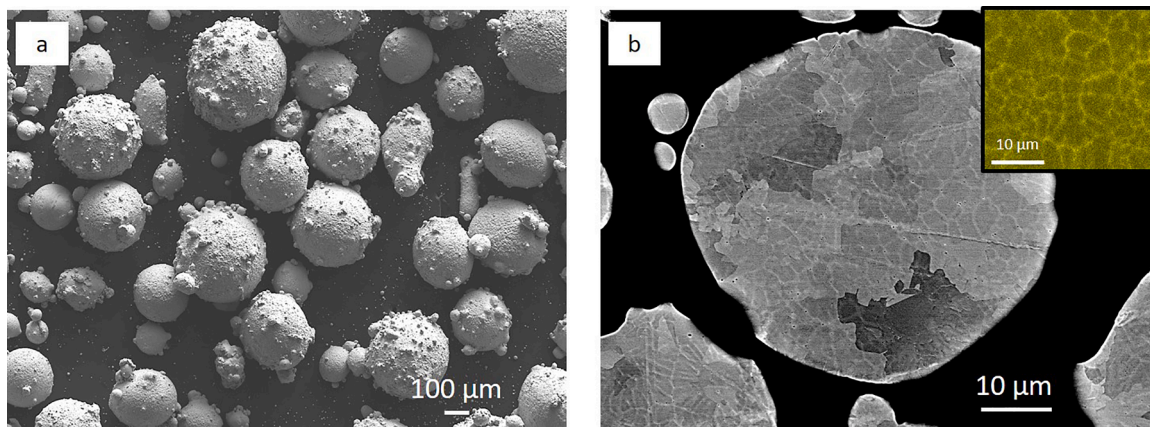


Fig. 1. SEM micrographs of 316 L uncoated powder. (a) Global view and (b) cross-section magnification of a particle. Inset: Ni EDS map.

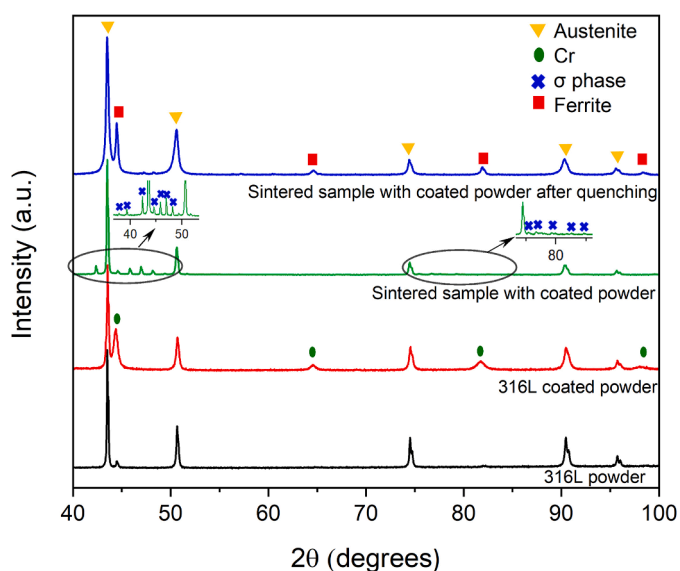


Fig. 2. XRD patterns of the investigated samples.

mechanical and corrosion properties comparable to conventional duplex stainless steels, without applying any annealing post-process treatment. They obtained promising results, except for ductility, which was lower compared to single-phase austenitic steel.

In parallel with AM techniques, pressure-assisted sintering processes, such as spark plasma sintering (SPS) and hot isostatic pressing (HIP), represent very interesting alternatives to conventional elaboration methods of metallic parts, such as casting and forging. In a recent work [19], a functionally graded material based on a ferritic low-alloyed steel and an austenitic stainless steel was obtained by mixing and consolidating different fractions of metallic powders via the HIP process. On the other hand, some works demonstrated the possibility of using also SPS route to quickly elaborate new materials with original/desired compositions [20–23]. Both SPS and HIP allow the elaboration of dense materials, with a fine-grained isotropic microstructure with improved durability properties [24–26], without requiring post-process heat treatments. Near-net-shape parts, with more or less complex geometries, can be obtained, reducing the machining costs [27–28]. In the HIP technique, the metal powder is inserted into a plastically deformable container, having a geometry close to the desired final shape. The container filled with the powder is then vacuum-drawn, sealed, and heated at high temperature (e.g. it can reach 2000 °C) while an isostatic pressure (up to 200 MPa) is simultaneously applied with an inert gas. However, a typical HIP cycle is quite long and can take several hours

[25]. On the other hand, in the SPS process, the powder is inserted into a graphite mold, and an electric current and a uniaxial pressure are simultaneously applied. The whole system is mainly heated by the Joule effect. The heating and cooling rates are of the order of several hundred °C·min<sup>-1</sup>: this contributes to reduce the grain growth [28–30]. Moreover, a holding time of 15 min is often enough to obtain sintered bulks with the required final density [28]. As a consequence, one of the advantages of the SPS technique over HIP is the rapidity of the process.

Based on previous information, SPS was then chosen in this study as an elaboration method for a new alloy design of a stainless steel with an austenitic-ferritic microstructure. The approach is innovative and not previously reported in the case of steel elaboration: instead of a pre-alloyed powder, or a mixture of powders of different nature, an austenitic 316 L powder coated by a chromium thin layer deposited by physical vapor deposition (PVD) technique was used in the present work as starting material. Plasma surface modification is an approach already used in the case of the functionalization of nanoscale particulate materials [31], but, to the best of the authors' knowledge, it was never applied to micrometric metallic powders. Some of the most important advantages of the PVD technique are the possibility to control the film thickness and obtain a uniform cover of the surfaces, even in the case of complex shapes [32]. It is known that chromium is an alpha-genic element that stabilizes the ferrite phase [33]. The underlying idea of the present work is that during the SPS process chromium diffusion occurs, promoting the nucleation of the ferrite phase and leading to the final elaboration of a two-phase austenitic-ferritic microstructure. Accurate characterizations were carried out, from the starting coated powder to the sintering products, and were completed by the simulation of film growth. Moreover, the effect of a thermal treatment after SPS was evaluated. The aim of the present study is double: on the one hand, to prove the possibility of performing the surface modification of a micrometric metallic powder by PVD technique and, on the other hand, to give first results concerning the possibility of considering the use of coated powder as an alternative to more conventional existing approaches, based on the use of pre-alloyed powders or a mixture of powders of different nature, for the development of new steel grades. The main advantage of a such new method, once optimized, is the possibility to elaborate two-phase austenitic-ferritic steels with a controlled amount of ferrite and austenite and, as a consequence, with improved durability properties.

## 2. Materials and methods

The 316 L powder used in this study was supplied by Aubert & Duval. Its composition is 0.015 C – 17.7 Cr – 1.88 Mn – 11.9 Ni – 2.44 Mo – 0.83 Si – 0.0117 O – bal. Fe (in wt.%). The powder was obtained by gas atomization and the particle's size ranges from 20 to 500 μm. Prior to

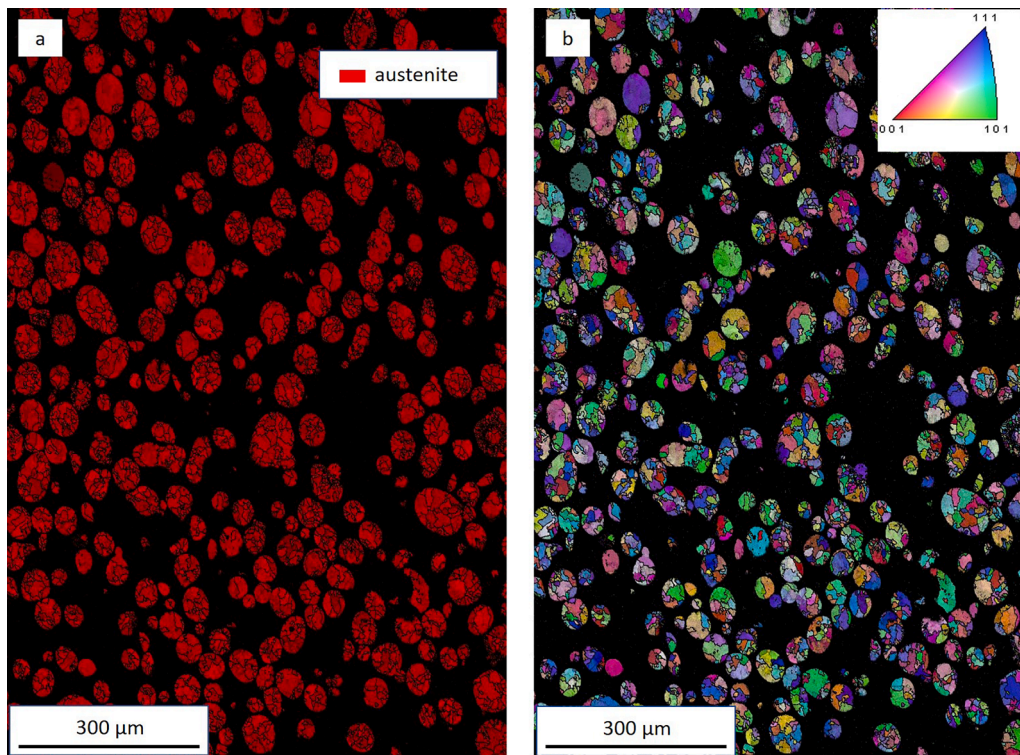


Fig. 3. EBSD maps of 316 L particles. (a) Phase map and (b) IPF map.

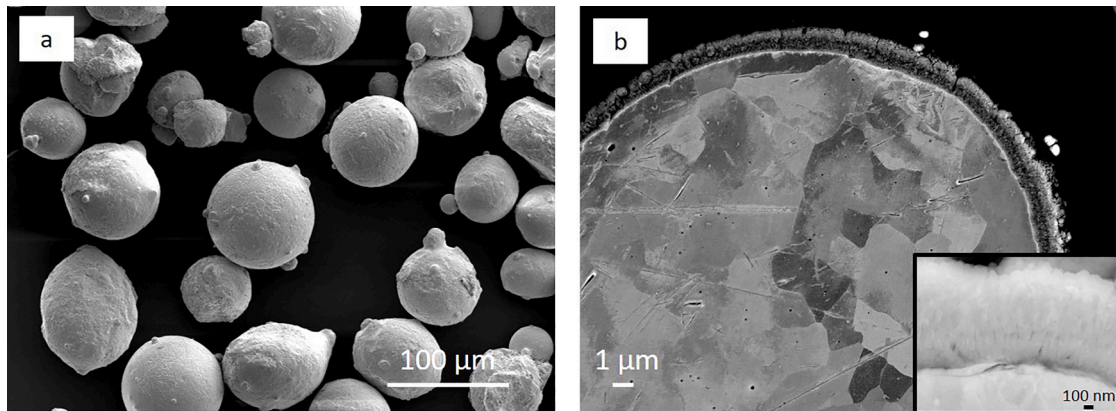


Fig. 4. SEM micrographs of 316 L coated powder. (a) Global view and (b) cross-section magnification of a particle. Inset: SEM magnification of the Cr coating.

deposition, the powder was sieved to reach a particle's size between 60 and 90  $\mu\text{m}$ .

Chromium coating on 316 L powder particles was synthesized by a DC magnetron sputtering system using a circular (50.8 mm in diameter, 6 mm thick) chromium metallic target (purity 99.99 %). The 90 g of powder was contained in a cylindrical container (60 mm in diameter and 100 mm in length) and continuously stirred during deposition to ensure a complete covering of each individual particle. Before deposition, the chamber was pumped down to reach a residual pressure of  $3.6 \cdot 10^{-3}$  Pa. An RF Ar etching was performed at 3 Pa, and the deposition took place at 1 Pa to achieve an expected film thickness of around 0.75  $\mu\text{m}$  (see supplementary materials S1, for a thickness distribution obtained from more than 150 measurements). According to the deposition process analyses and the chemical measurements, a mass of chromium around 4.5 g was deposited on the 90 g of powder.

Samples were sintered using an SPS HPD 10 apparatus (FCT system, Germany). A cylindrical graphite mold of 30 mm inner diameter, 90 mm

outer diameter, and 50 mm height was filled with the coated 316 L powder (about 28 g) to obtain a disk of 30 mm in diameter and 5 mm in height. Sintering was performed at 1100  $^{\circ}\text{C}$  for 15 min in vacuum (10–2 mbar) under a pressure of 70 MPa. The heating and the cooling rate were 50  $^{\circ}\text{C}\cdot\text{min}^{-1}$  and more than 100  $^{\circ}\text{C}\cdot\text{min}^{-1}$ , respectively.

Annealing treatment, followed by water quenching, was performed in a muffle furnace under Ar flow, at 1100  $^{\circ}\text{C}$  for 30 min, 1 and 2 h.

The starting powder, the sintered samples, and the quenched samples were cut, embedded in resin, and polished using SiC papers (down to 1200 grit) and diamond paste (down to 1  $\mu\text{m}$ ). Microstructural and elementary analyses were performed with a JEOL JSM-7600F scanning electron microscope (SEM) equipped with a field emission gun (FEG) and coupled with an energy-dispersive X-ray spectrometer (EDS). A Bruker D8-A25 diffractometer with Cu K $\alpha$  ( $\lambda = 0.154056$  nm) was used for phase identification. Phase quantification was performed by the Rietveld method. EBSD phase and inverse pole figure (IPF) maps of the initial powders and the sintered and quenched samples were acquired by



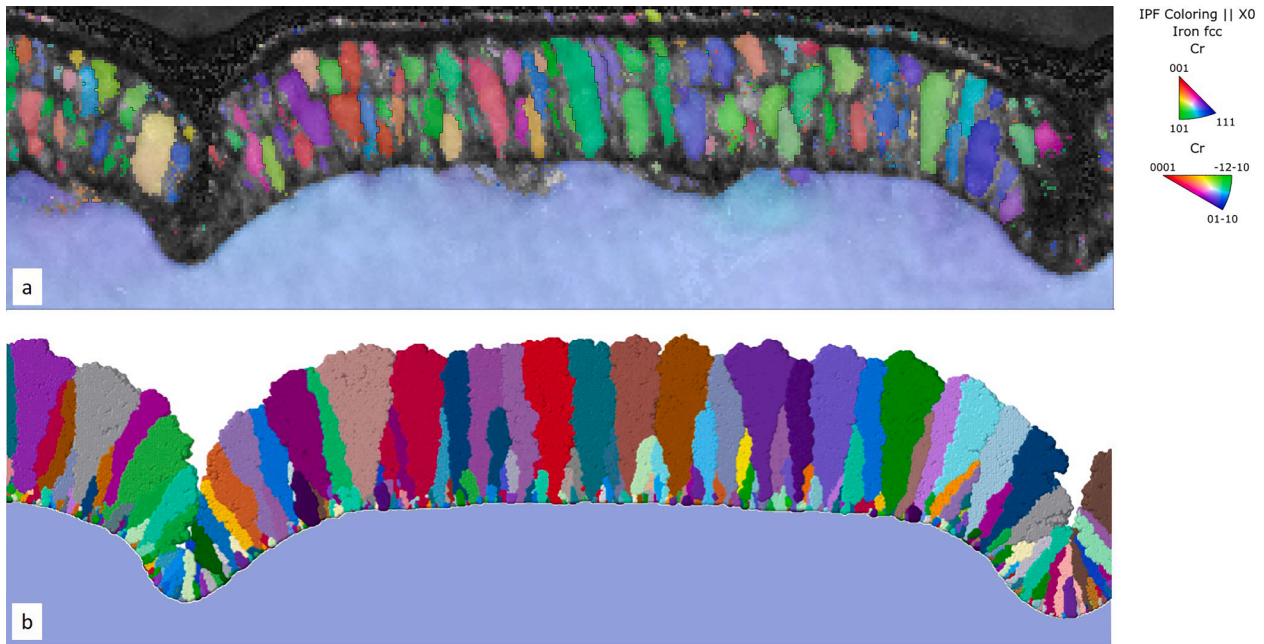


**Fig. 5.** (a) TKD orientation map (inverse pole figure along X direction) of Cr-coated 316 L powder; (b) simulated film growth (the colors represent different columns).

an SEM JEOL JSM-7600F coupled with an EDAX-TSL acquisition system and Ametek Digiview V camera.

A thin cross-section of the coated powder for transmission Kikuchi diffraction (TKD) and transmission electron microscopy (TEM) analyses was prepared by focused ion beam (FIB) using a Thermo Fischer HeliosNanoLab 600i apparatus and gallium ions. The TKD analyses were performed using a FEG-SEM JEOL JSM-7100F TTLS LV equipped with a CMOS EBSD camera (Symmetry S2, Oxford Instruments) and operating at an accelerating voltage of 30 kV. A JEOL JEM-2100F operating at an accelerating voltage of 200 kV was used for TEM characterizations.

Hardness measurements were performed on sintered and quenched samples with a Vickers indenter and a load of 100 gf (0.98 N) using a Wilson Tukon 1102/1202 tester.

The characteristic of the Cr flux was calculated with SiMTRA [34] using the experimental working pressure and system geometry. The initial angular and energy distribution was obtained by SRIM [35] using the experimental ion energy. The film growth was then simulated with the Virtual Coater NASCAM (v4.8.1, UNamur, Namur, Belgium) [36]. The profile of the substrate was extracted from SEM images and converted into a NASCAM substrate using the plug-in “Make substrate” with dimensions of  $10 \times 2602$  particles. In these simulations, a particle represents a volume with a side length of 4 nm. A total of  $2.5 \cdot 10^6$  particles were deposited. The segmentation in individual columns was made by an internal code [37].

### 3. Results and discussion

#### 3.1. Characterization of uncoated and coated 316 L powder

Uncoated 316 L powder particles are almost spherical (Fig. 1(a)). A significant number of small satellite particles are attached to the big ones, as typically observed for gas-atomized powders [38]. The cross-section observation of a single particle (Fig. 1(b)) shows the presence, inside the particle, of a network of fine metallurgical subgrains, separated by nickel segregations (Fig. 1(b) inset).

XRD analysis (Fig. 2- black pattern) revealed that the 316 L powder is almost completely austenitic, with only small traces (about 3 %) of ferrite. This result was confirmed by the EBSD phase map (Fig. 3(a)). On the other hand, EBSD inverse pole figures map along the Z direction

(IPF) (Fig. 3(b)) illustrates that the subgrains forming the 316 L particles are isotropic.

The particle’s size ranges from 20 to 500  $\mu\text{m}$ , but for the following of the study a tighter distribution, between 60 and 90  $\mu\text{m}$ , was chosen.

316 L particles coated by a chromium PVD layer are shown in Fig. 4 (a). The particles are uniformly coated and neither spalling nor cracks can be observed, an indication of the good adhesion of the chromium on the 316 L. Fig. 4(b) illustrates the cross-section magnification of one coated particle: the chromium coating is about 1  $\mu\text{m}$  thick and well adherent to the substrate.

SEM observation of the coating at higher magnification (Fig. 4(b) inset) showed that the coating presents a typical columnar morphology and that columns are formed by nanometric crystallites.

XRD analysis of the coated powder, performed on a batch of powder (Fig. 2- red pattern), confirmed the presence of austenite, as base material, and pure chromium, revealing that the chromium coating is completely crystallized. The intensity of the chromium peaks is lower than those of the austenite due to the smaller diffraction volume.

To more carefully characterize the coating, a thin foil was prepared by the FIB technique. The lamella was directly cut out of the surface of a coated particle, as illustrated in supplementary material S2. TKD orientation maps of Cr-coated 316 L powder are shown in Fig. 5(a), together with the simulation of the film growth (Fig. 5(b)).

The Cr PVD film is isotropic and columnar. It is also possible to observe that columns are formed by nanometric crystallites (Fig. 5(a)), as already evidenced by SEM analyses. For this particle, the thickness of the film is about 500 nm. The dark areas inside the film correspond to not indexed zones, presenting a coherent domain size lower than 10 nm, i.e. the step size used for TKD analysis. Moreover, a dark, not indexed, nanometric layer can be observed at the top surface of the film, between the columnar coating and the extreme surface. This amorphous layer is certainly an artifact due to FIB lamella preparation. The film is composed of monocrystalline columns of different sizes with small disorientations with a domain size of a few tenths of nm. The simulation of the film growth (Fig. 5(b)) reproduces well the columnar microstructure. At the bottom of the film, small columns are observed, not indexed by TKD, and corresponding to the initial growth competition of the clusters at the surface of the substrate. The covering of the substrate is respected, as the inclination of the columns in the two depressions

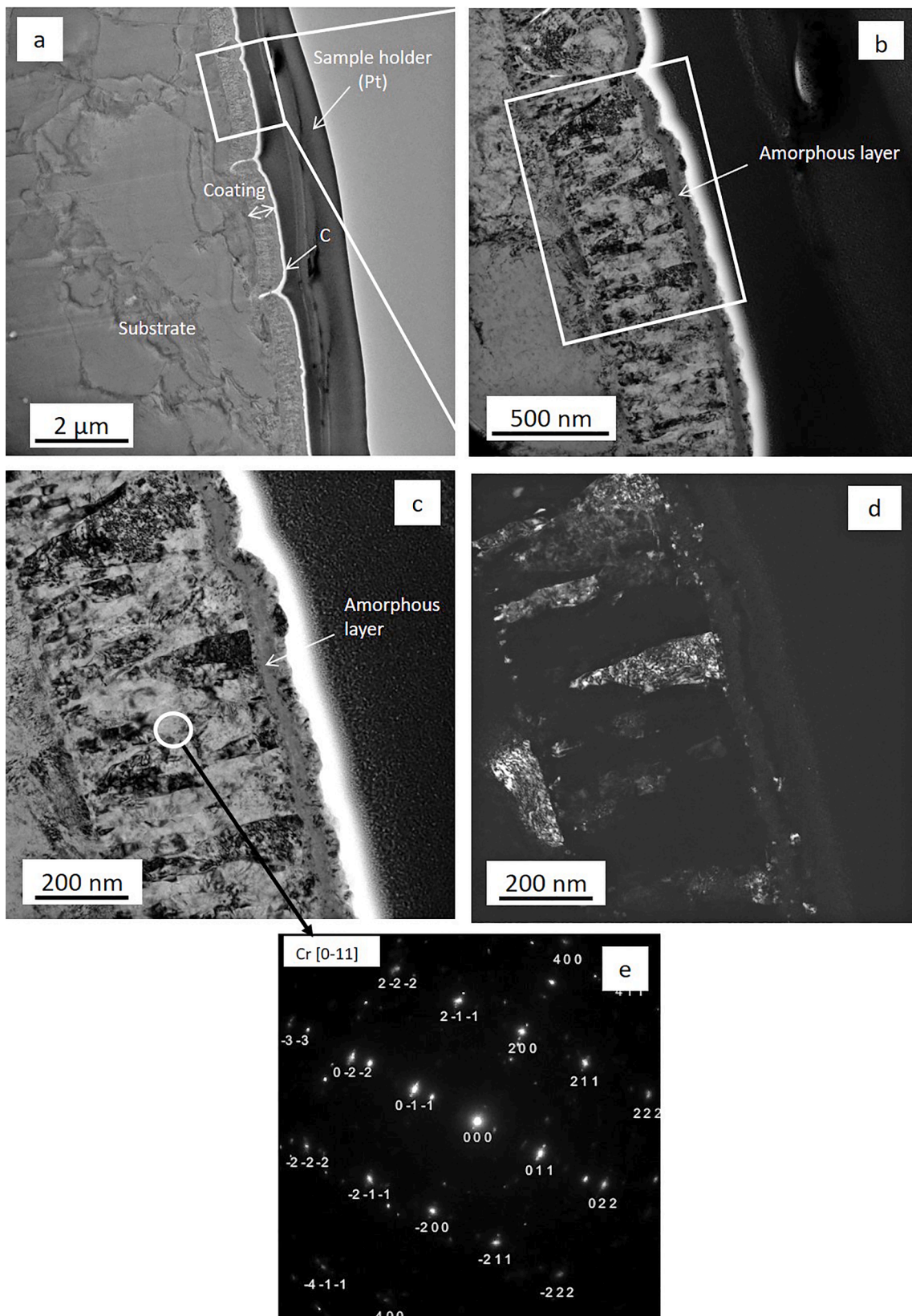


**Fig. 6.** TEM images of the Cr-coated 316 L powder lamella. (a) Global view; (b) magnification of a selected area; (c) bright field image of the zone evidenced in (b); (d) dark field image of the zone evidenced in (b); (e) diffraction patterns of bcc Cr phase.



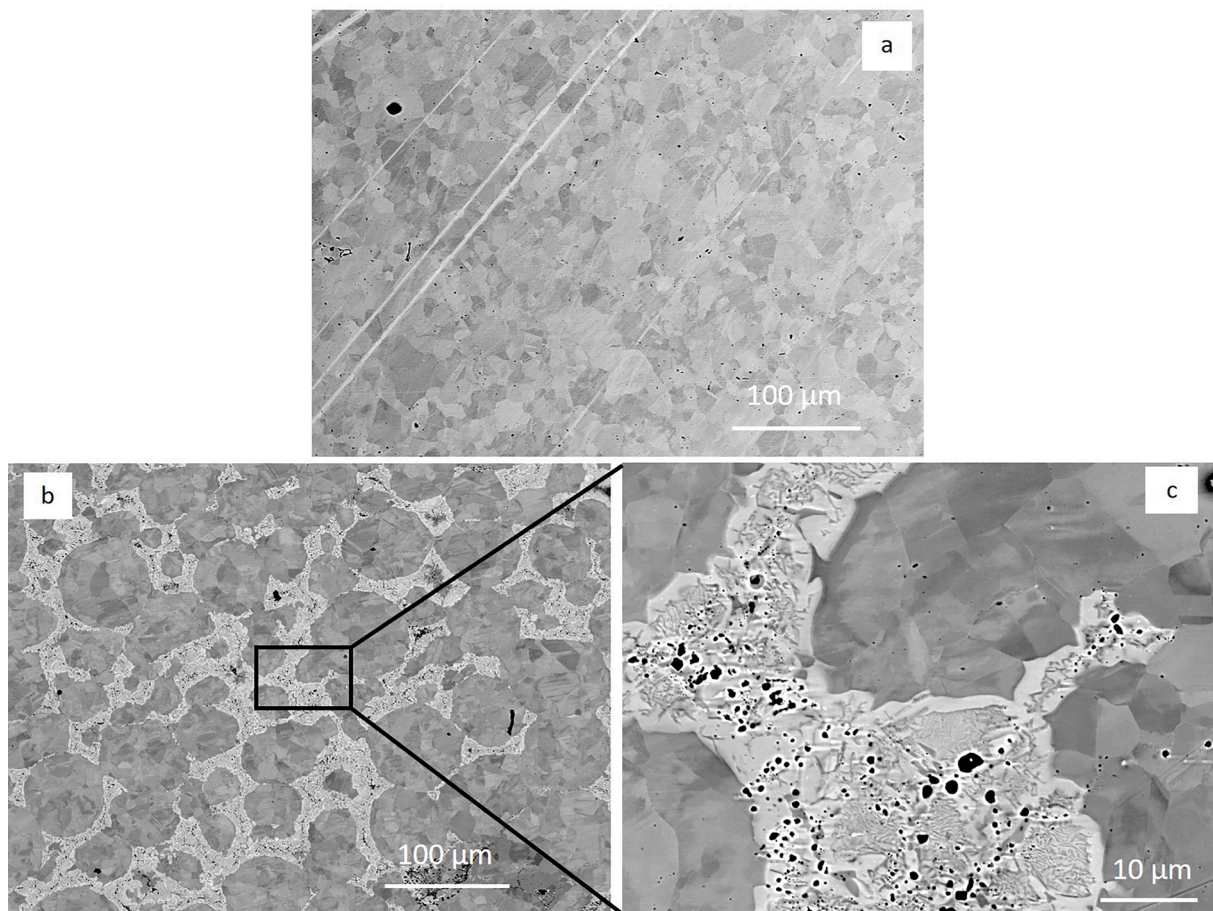


**Fig. 7.** Backscattered electron micrographs of sintered samples (a) with uncoated 316 L powder; (b) with Cr-coated 316 L powders and (c) magnification of the selected area in (b).

(certainly dendritic grain boundaries originating from the atomization). Moreover, in these two zones, the columns are small and inclined and consequently composed of even smaller coherent domain sizes.

To better characterize the coating, TEM analyses were then performed. Images of the thin Cr-coated 316 L powder lamella are presented in Fig. 6. The columnar structure is visible, as well as the presence, inside each column, of nanometric crystallites having a size lower than 10 nm, as mainly evidenced by the dark field image (Fig. 6(d)). Fig. 6(b) and (c) confirm the presence, in the upper part of the coating, of a layer of about 30 nm of thickness, having a different morphology compared to the coating, which is not indexed in the TKD orientation maps. As explained, this layer is amorphous and is an artifact formed during lamella preparation by the FIB technique. Selected area electron diffraction (SAED) analyses (Fig. 6(e)) were performed inside the coating (circle in Fig. 6(c)). The indexing of the diffraction patterns corresponds to bcc Cr with a [0-11] zone axis.

TEM-EDS local analyses of the film and the powder particles were performed, as well as EDS maps of major elements (Cr, Fe, Ni, and Mo - see supplementary materials S3), demonstrating, as expected, that no significant elementary diffusion (neither from the film to the powder nor from the powder to the film) occurred during PVD coating deposition.

### 3.2. Sintering of Cr-coated 316 L powder

The microstructures of the samples sintered with uncoated and Cr-coated 316 L powder are presented in Fig. 7.

The sample sintered with uncoated 316 L powder shows a homogeneous microstructure formed by small equiaxed grains (Fig. 7(a)). The initial powder particles are no longer visible.

On the other hand, after sintering with Cr-coated particles, the initial 316 L particles are still visible (Fig. 7(b)). Light grey zones formed at prior particle boundaries (PPB), creating a network between the initial powder particles. A very fine microstructure formed by an alternation of light and dark grey lamellae (Fig. 7(c)), typical of a eutectoid transformation, is visible inside the PPB zones, as well as some black spherical grains. EDS elementary maps (Fig. 8) reveal that the PPBs are enriched in chromium and molybdenum and depleted in iron and nickel. On the other hand, the black spherical grains correspond to manganese-enriched and silicon-enriched oxides. These maps also confirm that the dark grey zones are composed of Fe, Ni, Cr, Mo, and Mn, as expected for the 316 L particles.

EDS line scanning across a PPB was performed (see supplementary materials S4). Inside this area, the average chromium content is about 30 wt.% and it is quite constant. On the other hand, molybdenum content ranges between 2.3 and 3.3 wt.%. Both chromium and molybdenum wt.% are higher than the powder nominal contents of 17.7 and 2.44 wt.%, respectively. Manganese value varies from about 1 to 2 wt.% all along the scanned line and silicon content ranges from about 0.8 to 1.2 wt.%. Inside the PPB area, manganese and silicon values are locally slightly higher than the powder nominal contents of 1.88 and 0.78 wt.%, respectively. It is worth noting that inside the PPB zone, manganese and silicon follow the same trend as molybdenum. Nickel and iron show quite constant values inside the PPB zone, about 7 and 55 wt.%, respectively. These values are lower than the nominal contents of 11.9 and 65 wt.%. Due to the nanometric lamellae size, it was not possible to determine exactly their elementary composition by SEM-EDS. However, the line scanning shows that the amount of molybdenum sharply increases in the light grey lamellae and in the light grey area inside and



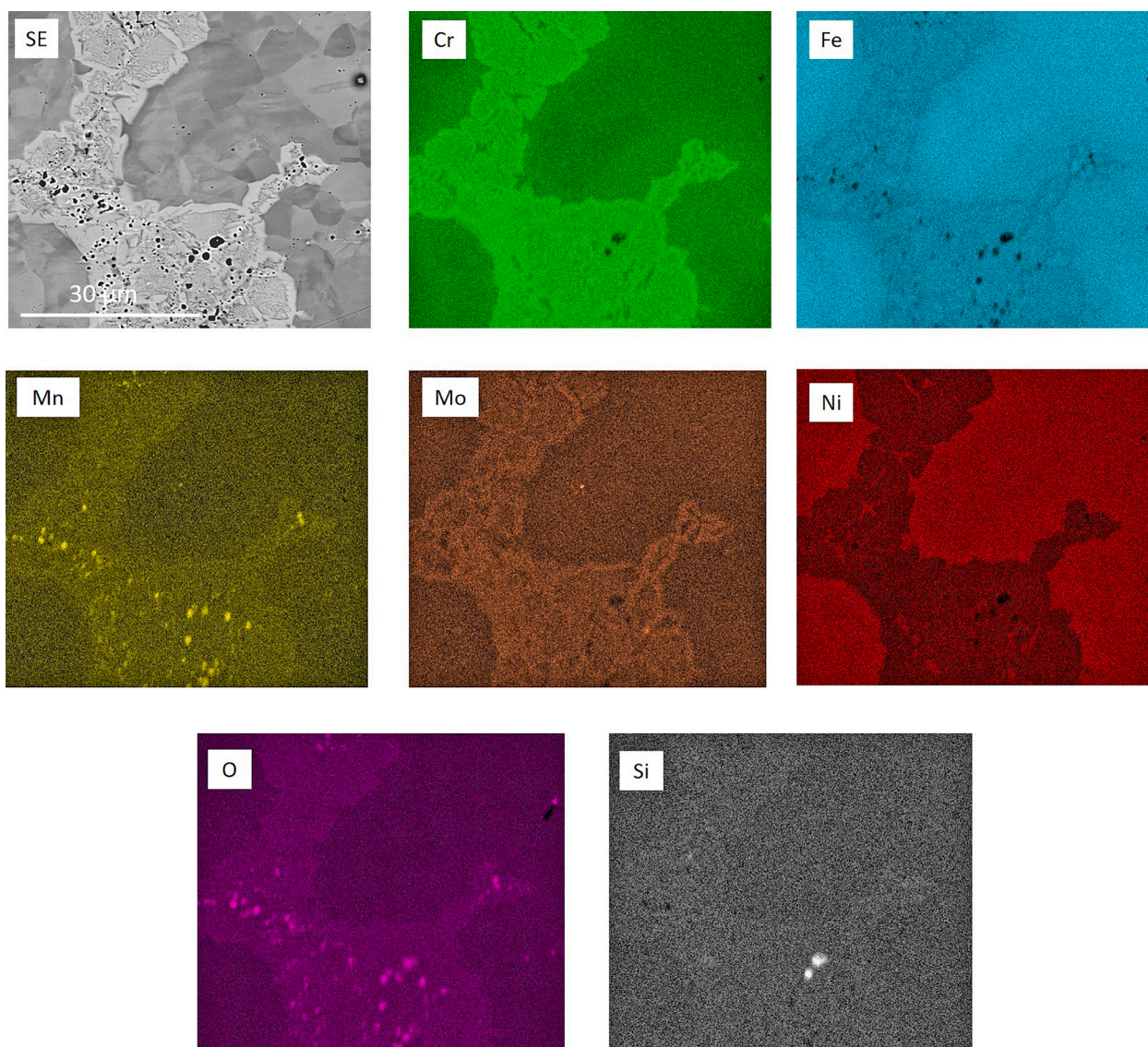


Fig. 8. EDS elementary maps of the sample sintered using Cr-coated powder.

around the PPB, respectively. Manganese and silicon values follow the same tendency. XRD analyses (Fig. 2- green pattern) revealed that the sintered sample contains austenite (77.5 %) and a tetragonal  $\sigma$ -type phase (22.5 %). It is known that the  $\sigma$  phase is an intermetallic Fe-Cr phase with a tetragonal crystal structure. Its precipitation is typically observed between 600 and 1000 °C [39,40]. As reported by Hsieh et al. [41],  $\sigma$  phase formation can occur for a Cr content of about 25–30 wt.% and is enhanced by the presence in stainless steel of ferrite stabilizers (chromium, silicon, or molybdenum). For this reason,  $\sigma$  phase composition is variable in the case of high alloyed steels but typically contains higher amounts of chromium and molybdenum than the matrix [42,43]. In the case of the present study, it is possible to claim that the  $\sigma$  phase corresponds to the light grey areas surrounding the PPB zones and to light grey lamellae inside the PPB areas. Lattice parameters for the Cr-Fe  $\sigma$  phase reported in the literature are  $a_0 = 8.799$  and  $c_0 = 4.544$  [41], which are very similar to the values found by XRD in the present work, which were  $a_0 = 8.791$  and  $c_0 = 4.578$ . The slight difference can be explained by the presence in the  $\sigma$  phase crystal lattice of atoms different from Cr and Fe, notably Mo, Si, and/or Mn atoms, as evidenced by EDS analysis.

In order to verify these hypotheses and to try to determine the nature of the light grey lamellae inside the PPB areas, EBSD phase and

orientation maps were performed (Fig. 9).

EBSD phase map (Fig. 9(a)) confirms that the  $\sigma$  phase formed in the outer part and inside the PPB zones, where it likely corresponds to light gray lamellae. Grey lamellae inside the PPB can be identified as austenite (Fig. 9(c)). Some sporadic ferritic grains were also revealed. Austenite and  $\sigma$  phase percentages found with EBSD analyses are in very good agreement with the results of XRD quantification. EBSD orientation map (Fig. 9(b)) displays that the sintered material is isotropic.

In duplex ferritic-austenitic stainless steels,  $\sigma$  phase generally precipitates at  $\delta$ -ferrite/ $\gamma$ -austenite grains boundaries, following the eutectoid reaction  $\delta$ -ferrite =  $\sigma$  +  $\gamma$ -austenite<sub>new</sub>, where  $\gamma$  austenite<sub>new</sub> is called new austenite [41,44]. Following this mechanism,  $\delta$ -ferrite can be completely consumed by  $\sigma$  phase formation.  $\sigma$  phase can also form in  $\gamma$ -austenite if the steel does not contain  $\delta$ -ferrite. However, in these conditions,  $\sigma$  phase formation is extremely low and takes a long time (of the order of some thousand hours at 700–750 °C) [45,46]. Finally,  $\sigma$  phase may precipitate into  $\delta$ -ferrite grains, due to the high Cr content of these regions, but this is the most difficult formation mechanism [45]. In the present study, due to the innovative approach, the situation is completely different from what can be typically found in literature, where the initial matrix can be ferritic-austenitic, only austenitic, or only ferritic. Indeed, in the present work, the initial powder is austenitic,



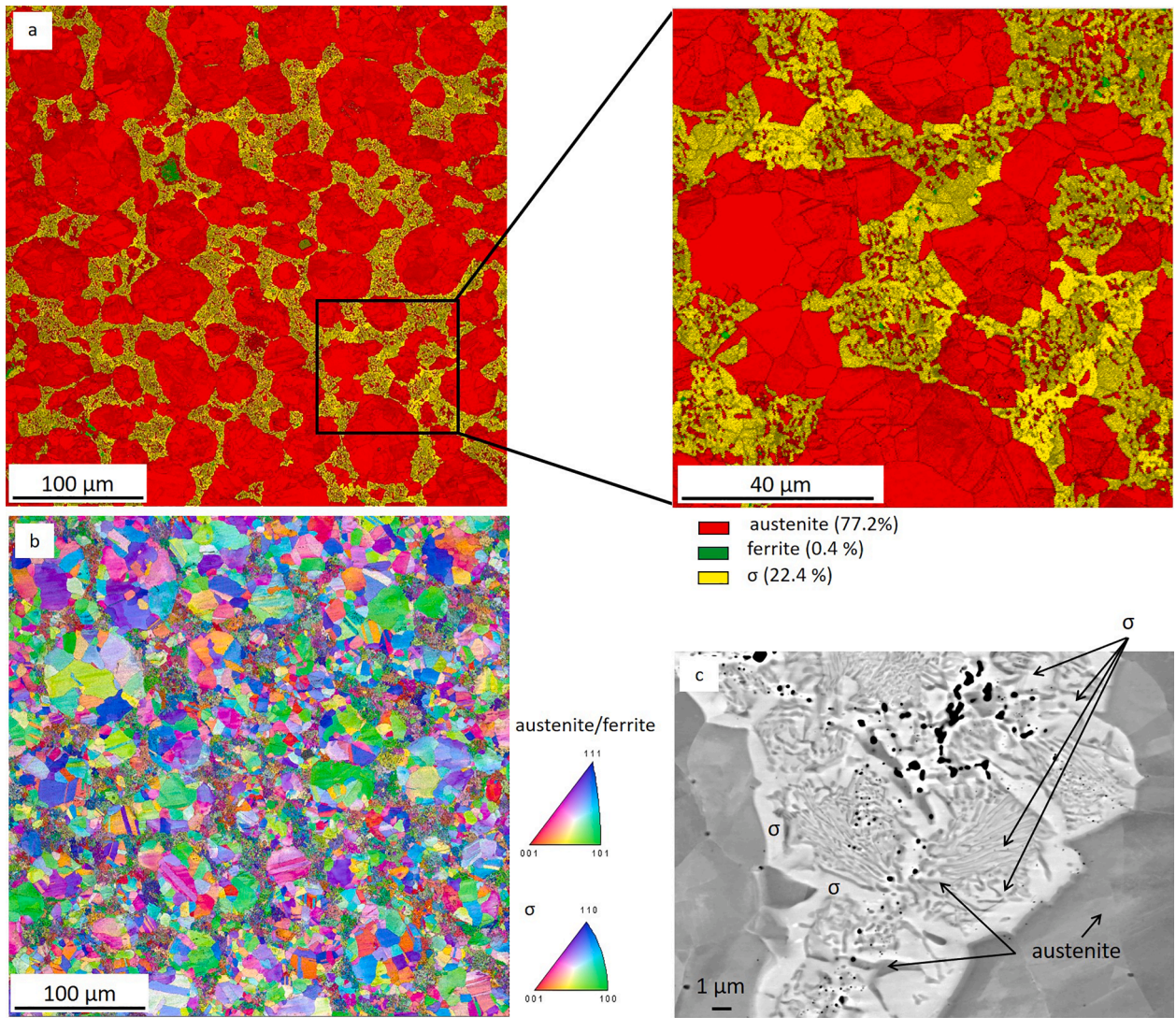


**Fig. 9.** EBSD maps of the sample sintered using Cr-coated powder. (a) Phase map; (b) orientation map (along Z direction); (c) backscattered electron micrograph showing the phases' repartition.

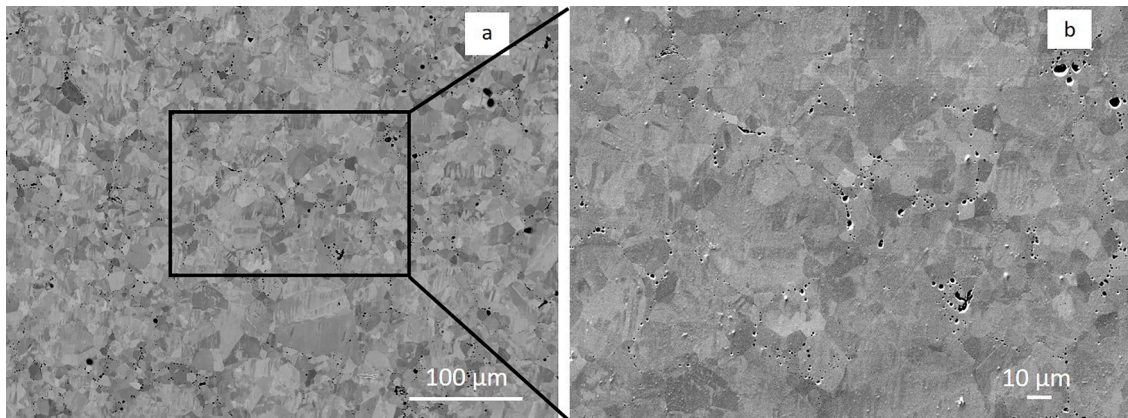


**Fig. 10.** Backscattered electron micrographs of the sample sintered with Cr-coated 316 L powder, heat-treated for 1 h at 1100 °C, and water quenched. (a) Global view; (b) magnification.

and pure chromium, a ferrite stabilizer element enhancing  $\sigma$  phase formation, was deposited on the surface of the austenitic particles and diffused during the high-temperature dwell. Consequently, every kind of

mechanism suggested for austenitic stainless steels does not apply to the present study. However, among the previously described mechanisms for  $\sigma$  phase formation, the only likely one is the eutectoid reaction



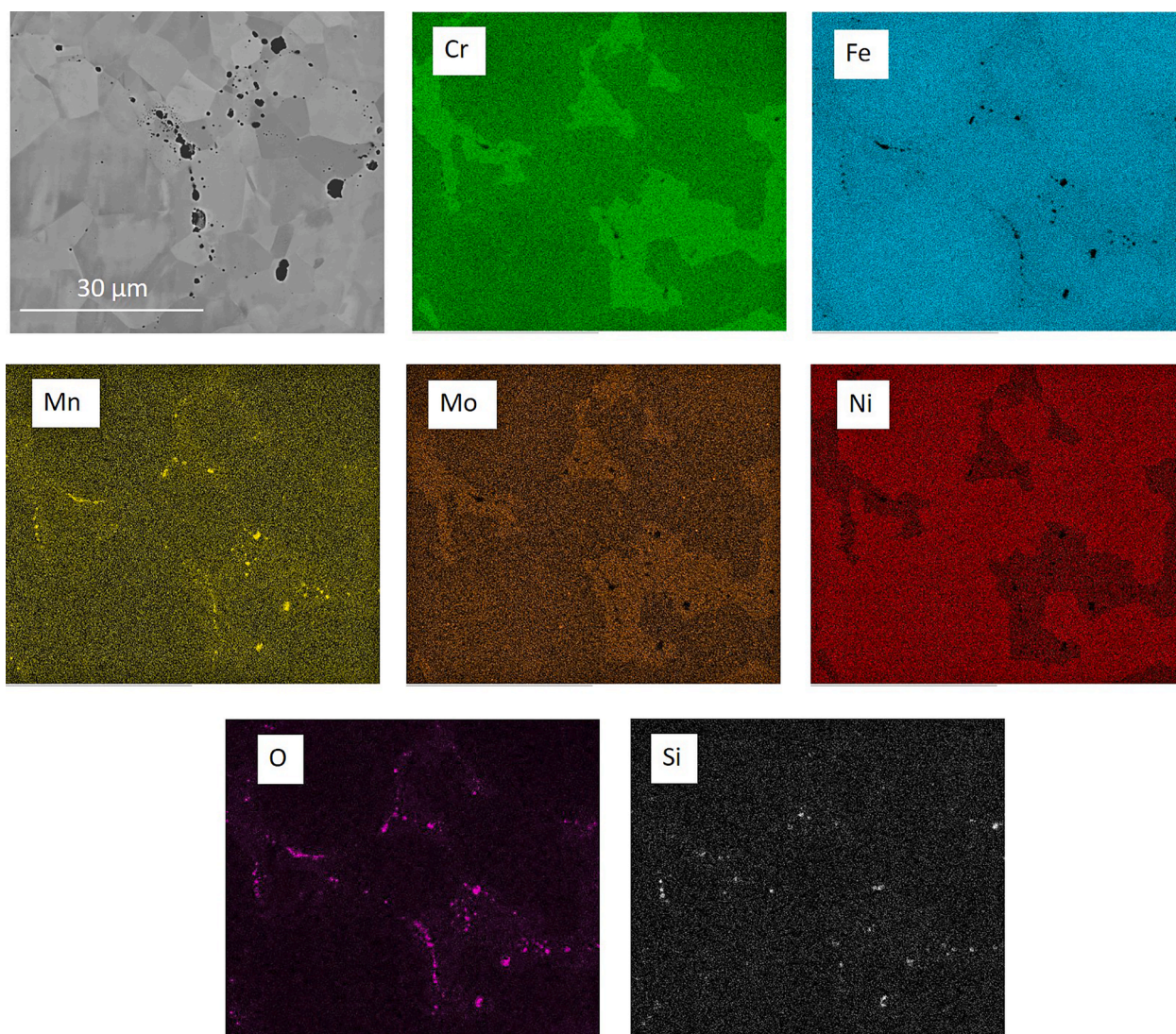


Fig. 11. EDS elementary maps of the sample sintered using Cr-coated powder, heat-treated for 1 h at 1100 °C, and water quenched.

$\delta$ -ferrite =  $\sigma$  +  $\gamma$ -austenite<sub>new</sub>. Indeed, it explains the lamellar eutectoid microstructure observed inside the PPB regions, formed by  $\sigma$  phase and austenite. This hypothesis is also supported by the presence of residual ferrite inside PPB, visible in the EBSD phase map (Fig. 9(a)). Following this mechanism, the precipitation of the  $\sigma$  phase would take place during cooling down, meaning that the cooling rate (about 250 °C.min<sup>-1</sup> from 1100 to 600 °C) during the SPS process is not fast enough to avoid  $\sigma$  phase formation. The equilibrium isopleth section of 316 L alloy in function of Cr mass-fraction was calculated (see supplementary material S5). Even if the eutectoid reaction is not visible, the isopleth section shows that the phases formed during cooling from sintering temperature (1373 K) to room temperature are FCC austenite, BCC ferrite and sigma, corroborating the previous results. Hardness measurements were performed in PPB zones and revealed a mean value of 525 HV0.1 ± 135, while the mean hardness of the austenitic matrix is 200 HV0.1 ± 4.  $\sigma$  phase formation increases drastically the hardness and has detrimental effects on material toughness and creep properties, mainly when precipitation occurs at grain boundaries [47,48].

### 3.3. Dissolution of $\sigma$ phase

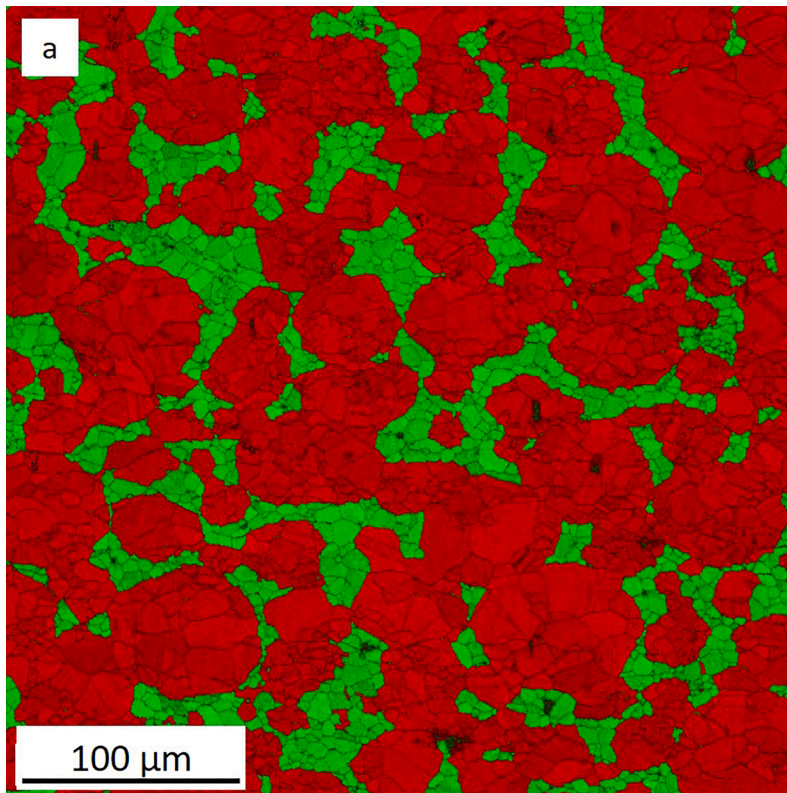
To promote  $\sigma$  phase dissolution, the sintered samples were heat-treated at 1100 °C for different times (30 min, 1, and 2 h) and then

water quenched. This temperature was chosen based on a study by Lu et al. [49]. For the three tested times, XRD analyses revealed the presence of austenite and ferrite (Fig. 2- blue pattern and supplementary materials S6) in quite the same proportion (around 21 % ferrite and 79 % austenite). This means that after thermal treatment the totality of the  $\sigma$  phase in the sintered sample transformed into ferrite and the whole austenite proportion was conserved. As the thermal treatment duration did not have any evident effect on the grain growth (see supplementary material S7), only the sample heat-treated for 1 hour will be presented thereafter. Fig. 10 displays the microstructure of the sintered sample after 1 h at 1100 °C and water quenched.

Initial powder particles are less visible compared to the sintered sample without post-treatment (Fig. 7) and the microstructure observed in backscattered electron mode appears more homogeneous. EDS elementary maps (Fig. 11) allow to identify PPB zones. As observed for the sintered not heat-treated sample, PPB regions, previously containing  $\sigma$  phase, are enriched in chromium and molybdenum and depleted in iron and nickel. Manganese-enriched and silicon-enriched oxides are also still observable.

EDS line scanning across a PPB (see supplementary materials S8) revealed that the chemical composition was identical to the one of the  $\sigma$ -phase before heat treatment. Indeed, inside PPB regions, chromium and molybdenum contents are about 30 and 3 wt.%, respectively.





■ austenite (76 %)
   
■ ferrite (24 %)

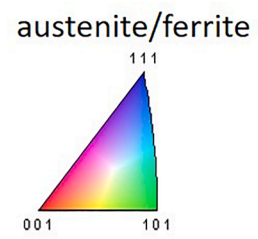
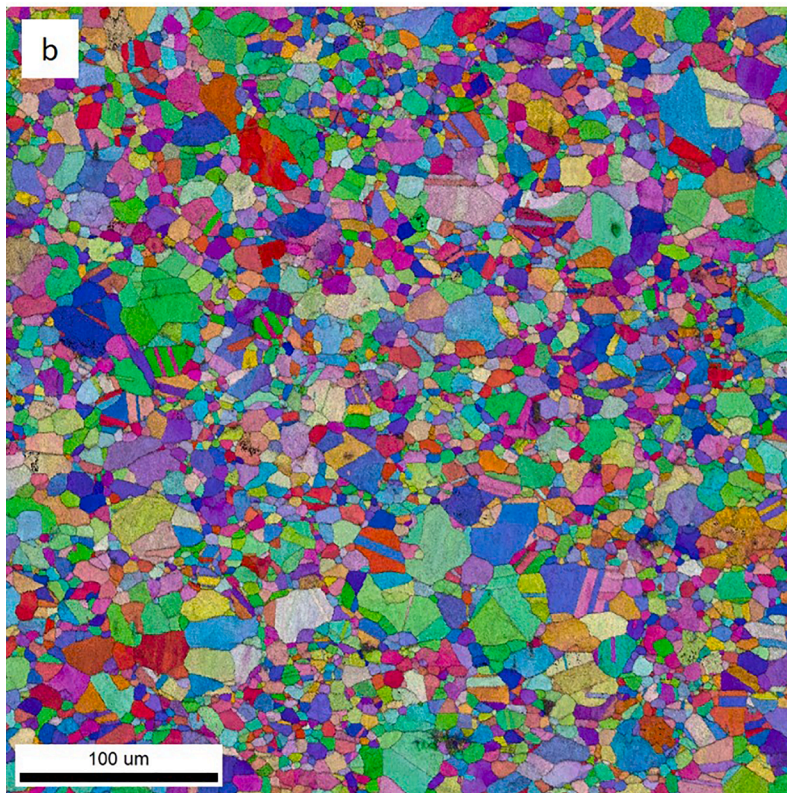


**Fig. 12.** EBSD maps of the sample sintered using Cr-coated powder, heat-treated for 1 h at 1100 °C, and water quenched. (a) Phase map and (b) orientation map (along Z direction).

Manganese value ranges from about 1.3 to 2.3 wt.% all along the scanned line and silicon content varies from about 0.8 to 1.1 wt.%. As previously detected before heat treatment inside PPB areas, nickel and iron show quite constant values, about 8 and 57 wt.%, respectively. These results indicate that the transformation of the  $\sigma$ -phase to ferrite during heat treatment followed by water quenching is consistent with a displacive (diffusionless) mechanism [50]. Note that EDS analysis performed in the case of the samples heat-treated for 30 min and 2 h (see supplementary materials S9) gave the same results as the one observed for 1 hour of thermal treatment: ferrite has the same elementary composition as the  $\sigma$ -phase from which it transforms.

Fig. 12 displays the EBSD phase and orientation maps of the sintered sample heat-treated for 1 h at 1100 °C and then water quenched.

EBSD phase map (Fig. 12(a)) confirms that  $\sigma$  phase was completely replaced by ferrite in PPB regions. As for sintered not heat-treated sample, the percentages of austenite and ferrite given by EBSD analyses are in quite good agreement with the results of XRD quantification. EBSD orientation map (Fig. 12(b)) reveals that the sintered material after heat treatment and water quenching is always isotropic. The size of the ferritic grains is greater than the one of the  $\sigma$  phase previously forming the PPB regions, but globally smaller than the size of the grains inside the initial 316 L powder particles. Twins inside the austenitic grains can always be observed.

The heat treatment at high temperatures followed by water quenching is not only effective in suppressing the brittle  $\sigma$  phase but also allows to obtain, globally, a more homogeneous microstructure, suggesting better durability properties.

Finally, it is worth noting that the Cr coating on the particles' surface before SPS and subsequent annealing had a thickness of 0.75  $\mu\text{m}$ . After SPS and annealing, the size of the ferritic areas (equal to the size of the interparticulate regions containing the sigma phase after SPS) reached 30  $\mu\text{m}$ , demonstrating the full diffusion of the Cr layer over a few tenths of  $\mu\text{m}$ . The present work illustrates that elemental composition is not stationary and Cr diffusion during SPS is very effective. The initial interfaces evolve consequently under the effect of complex diffusion phenomena occurring during SPS in a reactive, non-equilibrium system.

#### 4. Conclusions

In the present study, a 316 L austenitic powder coated by a thin chromium layer deposited by physical vapor deposition (PVD) technique was sintered by the SPS process. The aim is double: on the one hand, to prove the possibility of performing the surface modification of a micrometric metallic powder by PVD technique and, on the other hand, to give first results concerning the possibility of considering the use of coated powder as an alternative to more conventional existing approaches, based on the use of pre-alloyed powders or a mixture of powders of different nature, for the development of new steel grades. The main conclusions are listed below:

- TEM characterizations showed that chromium coating presents a columnar isotropic microstructure formed by nanometric crystallites. Its thickness ranges from 0.5 to 1  $\mu\text{m}$ .
- After SPS, the initial austenitic powder particles are still visible in the bulk microstructure. The tetragonal  $\sigma$  phase, enriched in chromium and molybdenum, forms in the interparticulate regions, where oxides containing mainly silicon and manganese are also detected.
- Due to the lamellar microstructure and to the presence of residual ferrite in the EBSD phase map,  $\sigma$  phase formation probably follows the eutectoid reaction  $\delta\text{-ferrite} = \sigma + \gamma\text{-austenite}$ , which indicates that the cooling rate during SPS process is not fast enough to avoid  $\sigma$  phase precipitation.
- A thermal treatment at 1100 °C (30 min, 1 and 2 h) followed by water quenching is effective in completely dissolving the  $\sigma$  phase: the totality of  $\sigma$  phase is transformed into ferrite and the whole austenite

proportion is conserved. The thermal treatment duration does not have any evident effect on grain growth.

- The chemical composition of the ferrite is the same as the one of the  $\sigma$  phase from which it forms, suggesting that  $\sigma$  to ferrite transformation follows a displacive mechanism.
- EBSD maps show that the size of the ferrite grains is bigger than the one of the  $\sigma$  phase, proving that heat treatment followed by water quenching is not only effective in suppressing the brittle  $\sigma$  phase but also allows obtaining, globally, a more homogeneous microstructure, suggesting better durability properties.

In the present preliminary study, it was chosen to work with a quite narrow distribution of powder particles sizes. However, further investigations are necessary to fully understand the influence of a broader powder particles size distribution. Additionally, as the present work has demonstrated that the Cr elemental diffusion during SPS is very effective, future studies will be conducted with powder coated with different Cr film thicknesses to explore the potential for increasing the ferrite/austenite phase fraction in the final material.

#### CRediT authorship contribution statement

**M.R. Ardigo-Besnard:** Conceptualization, Investigation, Validation, Resources, Writing – original draft, Project administration, Funding acquisition. **A. Besnard:** Conceptualization, Investigation, Validation, Writing – review & editing. **Y. Pinot:** Investigation, Writing – review & editing. **F. Bussi re:** Investigation. **J.-P. Chateau-Cornu:** Conceptualization, Resources. **C. Vandenebeele:** Investigation, Writing – review & editing. **S. Lucas:** Investigation, Writing – review & editing. **N. Watiez:** Investigation. **A. Descamps-Mandine:** Investigation, Writing – review & editing. **C. Josse:** Investigation, Writing – review & editing. **A. Proietti:** Investigation, Writing – review & editing.

#### Declaration of Competing Interest

The authors declare that they have no known competing financial interests or personal relationships that could have appeared to influence the work reported in this paper.

#### Data availability

The raw/processed data required to reproduce these findings cannot be shared at this time as the data also forms part of an ongoing study.

#### Acknowledgments

The authors wish to thank the Bourgogne-Franche-Comt  Region (project number 2020Y-19371) and the European Regional Development Fund (reference: PO FEDER-FSE Bourgogne 2014-2020) for their financial support of the THEMPO project, for the FIB, TEM, and TKD experiments.

#### Supplementary materials

Supplementary material associated with this article can be found, in the online version, at [doi:10.1016/j.mta.2023.102002](https://doi.org/10.1016/j.mta.2023.102002).

#### References

- [1] S. Papula, M. Song, A. Pateras, X.-B. Chen, M. Brandt, M. Easton, Y. Yagodzinskyy, I. Virkkunen, H. H nninen, Selective laser melting of duplex stainless steel 2205: effect of post-processing heat treatment on microstructure, mechanical properties, and corrosion resistance, *Metal. (Basel)* 12 (15) (2019) 2468–2483, <https://doi.org/10.3390/ma12152468>.



- [2] N. Ebrahimi, M. Momeni, M.H. Moayed, A. Davoodi, Correlation between critical pitting temperature and degree of sensitisation on alloy 2205 duplex stainless steel, *Corros. Sci.* 53 (2) (2011) 637–644, <https://doi.org/10.1016/j.corsci.2010.10.009>.
- [3] F. Hengsbach, P. Koppa, K. Duschik, M.J. Holzweissig, M. Burns, J. Nellesen, W. Tillmann, T. Tröster, K.-P. Hoyer, M. Schaper, Duplex stainless steel fabricated by selective laser melting - Microstructural and mechanical properties, *Mater. Des.* 133 (2017) 136–142, <https://doi.org/10.1016/j.matdes.2017.07.046>.
- [4] M. Knyazeva, M. Pohl, Duplex steels: part I: genesis, formation, structure, *Metallogr. Microstruct. Anal.* 2 (2013) 113–121, <https://doi.org/10.1007/s13632-013-0066-8>.
- [5] R.N. Gunn, *Duplex Stainless Steels: Microstructure, Properties and Applications*, Abington Publishing, Cambridge, England, 1997.
- [6] Y.Q. Wang, B. Yang, J. Han, F. Dong, Y.L. Wang, Localized corrosion of thermally aged cast duplex stainless steel for primary coolant pipes of nuclear power plant, *Procedia Eng.* 36 (2012) 88–95, <https://doi.org/10.1016/j.proeng.2012.03.015>.
- [7] J. Paro, H. Hanninen, V. Kauppinen, Tool wear and machinability of HIPed P/M and conventional cast duplex stainless steels, *Wear* 249 (3) (2001) 279–284, [https://doi.org/10.1016/S0043-1648\(01\)00570-1](https://doi.org/10.1016/S0043-1648(01)00570-1).
- [8] H. Xiang, W. Zhao, Y. Lu, Effect of solution temperature on microstructure and mechanical properties of selective laser melted Fe22Cr5Ni-0.26 N duplex stainless steel, *J. Mat. Res. Technol.* 19 (2022) 1379–1389, <https://doi.org/10.1016/j.jmrt.2022.05.124>.
- [9] Y. Zhang, S. Wu, F. Cheng, A duplex stainless steel (DSS) with striking tensile strength and corrosion resistance produced through wire arc-additive manufacturing (WAAM) using a newly developed flux-cored wire, *Mater. Lett.* 313 (2022) 131760–131765, <https://doi.org/10.1016/j.matlet.2022.131760>.
- [10] N. Haghadi, C. Ledermueller, H. Chen, Z. Chen, Q. Liu, X. Li, G. Rohrer, X. Liao, S. Ringer, S. Primig, Evolution of microstructure and mechanical properties in 2205 duplex stainless steels during additive manufacturing and heat treatment, *Mater. Sci. Eng. A* 835 (2022) 142695–142711, <https://doi.org/10.1016/j.msea.2022.142695>.
- [11] D. Zhang, A. Liu, B. Yin, P. Wen, Additive manufacturing of duplex stainless steels - a critical review, *J. Manuf. Process.* 73 (2022) 496–517, <https://doi.org/10.1016/j.jmapro.2021.11.036>.
- [12] K. Davidson, S. Singamneni, Selective laser melting of duplex stainless steel powders; an investigation, *Mater. Manuf. Process.* 31 (12) (2016) 1543–1555, <https://doi.org/10.1080/10426914.2015.1090605>.
- [13] J. Kunz, A. Boontanom, S. Herzog, P. Suwanpinij, A. Kaletsch, C. Broeckmann, Influence of hot isostatic pressing post-treatment on the microstructure and mechanical behavior of standard and super duplex stainless steel produced by laser powder bed fusion, *Mater. Sci. Eng. A* 794 (2020) 139806–139817, <https://doi.org/10.1016/j.msea.2020.139806>.
- [14] K.P. Davidson, S. Singamneni, The mechanics of machining selective laser melted super duplex stainless steels, *J. Mat. Res. Technol.* 17 (2022) 601–611, <https://doi.org/10.1016/j.jmrt.2022.01.025>.
- [15] D.M. Escriba, E. Materna-Morris, R.L. Plaut, A.F. Padilha, Chi-phase precipitation in a duplex stainless steel, *Mater. Character.* 60 (11) (2009) 1214–1219, <https://doi.org/10.1016/j.matchar.2009.04.013>.
- [16] N. Llorca-Isern, H. López-Luque, I. López-Jiménez, M.V. Biezma, Identification of sigma and chi phases in duplex stainless steels, *Mater. Character.* 112 (2016) 20–29, <https://doi.org/10.1016/j.matchar.2015.12.004>.
- [17] J. Michalska, M. Sozańska, Qualitative and quantitative analysis of  $\sigma$  and  $\chi$  phases in 2205 duplex stainless steel, *Mater. Character.* 56 (4–5) (2006) 355–362, <https://doi.org/10.1016/j.matchar.2005.11.003>.
- [18] M.L. Kohler, J. Kunz, S. Herzog, A. Kaletsch, C. Broeckmann, Microstructure analysis of novel LPBF-processed duplex stainless steels correlated to their mechanical and corrosion properties, *Mat. Sci. Eng. A* 801 (2021) 140432–140441, <https://doi.org/10.1016/j.msea.2020.140432>.
- [19] E. Stavroulakis, D. Bowden, S. Irukuvarghula, A. Garner, E. Pickering, D. Stewart, M. Preuss, Characterisation of ferritic to austenitic steel functional grading via powder hot isostatic pressing, *Mater. Today Commun.* 31 (2022) 103442, <https://doi.org/10.1016/j.mtcomm.2022.103442>.
- [20] V. Chaudhary, L.P. Tan, V.K. Sharma, R.V. Ramanujan, Accelerated study of magnetic Fe-Co-Ni alloys through compositionally graded spark plasma sintered samples, *J. Alloy. Compd.* 869 (2021) 159318–159325, <https://doi.org/10.1016/j.jallcom.2021.159318>.
- [21] A. Fourmont, S. Le Gallet, O. Politano, C. Desgranges, F. Baras, Effects of planetary ball milling on AlCoCrFeNi high entropy alloys prepared by spark plasma sintering: experiments and molecular dynamics study, *J. Alloy. Compd.* 820 (2020) 153448–153458, <https://doi.org/10.1016/j.jallcom.2019.153448>.
- [22] D. Monceau, D. Oquab, C. Estournes, M. Boidot, S. Selezneff, Y. Thebault, Y. Cadoret, Pt-modified Ni aluminides, MCrAlY-base multilayer coatings and TBC systems fabricated by spark plasma sintering for the protection of Ni-base superalloys, *Surf. Coat. Technol.* 204 (2009) 771–778, <https://doi.org/10.1016/j.surfcoat.2009.09.054>.
- [23] J. Zhang, B. Villero, B. Knosp, P. Bernard, M. Lacroche, Structural and chemical analyses of the new ternary La<sub>5</sub>MgNi<sub>24</sub> phase synthesized by spark plasma sintering and used as negative electrode material for Ni-MH batteries, *Int. J. Hydrog. Energy* 37 (2012) 5225–5233, <https://doi.org/10.1016/j.ijhydene.2011.12.096>.
- [24] A. Meza, E. Macia, P. Chekhonin, E. Altstadt, M.E. Rabanal, J.M. Torralba, M. Campos, The effect of composition and microstructure on the creep behaviour of 14 Cr ODS steels consolidated by SPS, *Mater. Sci. Eng. A* 849 (2022) 143441–143449, <https://doi.org/10.1016/j.msea.2022.143441>.
- [25] A. Tellier, M.R. Ardigo-Besnard, J.-P. Chateau-Cornu, R. Chassagnon, J.-M. Fiorani, Characterization of the interfacial zone Between a HIPed Fe-based alloy and a stainless steel container, *J. Mater. Eng. Perform.* 29 (2020) 3800–3811, <https://doi.org/10.1007/s11665-020-04897-5>.
- [26] M.R. Ardigo-Besnard, A. Tellier, A. Besnard, J.-P. Chateau-Cornu, Effect of the microstructure on the tribological properties of HIPed and PTA-welded Fe-based hardfacing alloy, *Surf. Coat. Technol.* 425 (2021) 127691–127700, <https://doi.org/10.1016/j.surfcoat.2021.127691>.
- [27] H.V. Atkinsons, S. Davies, Fundamental aspects of hot isostatic pressing: an overview, *Metal. Mater. Trans. A* 31 (2000) 2981–3001, <https://doi.org/10.1007/s11661-000-0078-2>.
- [28] Z.-Y. Hu, Z.-H. Zhang, X.-W. Cheng, F.-C. Wang, Y.-F. Zhang, S.-L. Li, A review of multi-physical fields induced phenomena and effects in spark plasma sintering: fundamentals and applications, *Mater. Des.* 191 (2020) 108662–108716, <https://doi.org/10.1016/j.matdes.2020.108662>.
- [29] Z.A. Munir, U. Anselmi-Tamburini, M. Ohyanagi, The effect of electric field and pressure on the synthesis and consolidation of materials: a review of the spark plasma sintering method, *J. Mater. Sci.* 41 (3) (2006) 763–777, <https://doi.org/10.1007/s10853-006-6555-2>.
- [30] V. Mamedov, Spark plasma sintering as advanced PM sintering method, *Powder Metall.* 45 (4) (2002) 322–328, <https://doi.org/10.1179/003258902225007041>.
- [31] C.R. Vandenebeele, S. Lucas, Technological challenges and progress in nanomaterials plasma surface modification – a review, *Mater. Sci. Eng. R* 139 (2020) 100521–100561, <https://doi.org/10.1016/j.mser.2019.100521>.
- [32] M. Evrard, A. Besnard, S. Lucas, Study of the influence of the pressure and rotational motion of 3D substrates processed by magnetron sputtering: a comparative study between Monte Carlo modelling and experiments, *Surf. Coat. Technol.* 378 (2019) 125070–125080, <https://doi.org/10.1016/j.surfcoat.2019.125070>.
- [33] A.P. Kölblinger, S.S.M. Tavares, C.A. Della Rovere, A.R. Pimenta, Failure analysis of a flange of superduplex stainless steel by preferential corrosion of ferrite phase, *Eng. Fail. Anal.* 134 (2022) 106098–106110, <https://doi.org/10.1016/j.engfailanal.2022.106098>.
- [34] D. Depla, W.P. Leroy, Magnetron sputter deposition as visualized by Monte Carlo modeling, *Thin. Solid. Film.* 520 (2012) 6337–6354, <https://doi.org/10.1016/j.tsf.2012.06.032>.
- [35] J.-F. Ziegler, SRIM-2003, *Nucl. Instrum. Method. Phys. Res. B* 219–220 (2004) 1027–1036, <https://doi.org/10.1016/j.nimb.2004.01.208>.
- [36] P. Moskovkin, S. Lucas, Computer simulations of the early stage growth of Ge clusters at elevated temperatures, on patterned Si substrate using the kinetic Monte Carlo method, *Thin Solid. Film.* 536 (2013) 313–317, <https://doi.org/10.1016/j.tsf.2013.03.031>.
- [37] N. Watez, A. Besnard, P. Moskovkin, R. Lou, J. Outeiro, H. Birembaux, S. Lucas, Finite element mesh generation for nano-scale modeling of tilted columnar thin films for numerical simulation. In: Noël, F., Nyffenegger, F., Rivest, L., Bouras, A. (eds) *Product Lifecycle Management. PLM in Transition Times: The Place of Humans and Transformative Technologies. PLM 2022. IFIP Advances in Information and Communication Technology*, vol 667 (2023). Springer, Cham. [https://doi.org/10.1007/978-3-031-25182-5\\_22](https://doi.org/10.1007/978-3-031-25182-5_22).
- [38] F. Chu, K. Zhang, H. Shen, M. Liu, W. Huang, X. Zhang, E. Liang, L. Lei, J. Hou, A. Huang, Influence of satellite and agglomeration of powder on the processability of AlSi10Mg powder in laser powder bed fusion, *J. Mater. Res. Technol.* 11 (2021) 2059–2073, <https://doi.org/10.1016/j.jmrt.2021.02.015>.
- [39] M.E. Wilms, V.J. Gadgil, J.M. Krougman, F.P. Ijsseling, The effect of  $\sigma$ -phase precipitation at 800 °C on the corrosion resistance in sea-water of a high alloyed duplex stainless steel, *Corros. Sci.* 36 (1994) 871–881, [https://doi.org/10.1016/0010-938X\(94\)90176-7](https://doi.org/10.1016/0010-938X(94)90176-7).
- [40] C.M. Souza, H.F.G. Abreu, S.S.M. Tavares, J.M.A. Rebello, The  $\sigma$  phase formation in annealed UNS S31803 duplex stainless steel: texture aspects, *Mater. Character.* 59 (2008) 1301–1306, <https://doi.org/10.1016/j.matchar.2007.11.005>.
- [41] C.-C. Hsieh, W. Wu, Overview of intermetallic sigma ( $\sigma$ ) phase precipitation in stainless steels, *ISRN Metall* 2012 (2012) 1–16, <https://doi.org/10.5402/2012/732471>.
- [42] N. Llorca-Isern, H. López-Luque, I. López-Jiménez, M.V. Biezma, Identification of sigma and chi phases in duplex stainless steels, *Mater. Character.* 112 (2016) 20–29, <https://doi.org/10.1016/j.matchar.2015.12.004>.
- [43] J. Michalska, M. Sozańska, Qualitative and quantitative analysis of  $\sigma$  and  $\chi$  phases in 2205 duplex stainless steel, *Mater. Character.* 56 (2006) 355–362, <https://doi.org/10.1016/j.matchar.2005.11.003>.
- [44] D.M. Escriba, E. Materna-Morris, R.L. Plaut, A.F. Padilha, Chi-phase precipitation in a duplex stainless steel, *Mater. Character.* 60 (2009) 1214–1219, <https://doi.org/10.1016/j.matchar.2009.04.013>.
- [45] Y.S. Na, N.K. Park, R.C. Reed, Sigma morphology and precipitation mechanism in Udimet 720Li, *Scripta Mater.* 43 (2000) 585–590, [https://doi.org/10.1016/S1359-6462\(00\)00441-3](https://doi.org/10.1016/S1359-6462(00)00441-3).
- [46] M.H. Lewis, Precipitation of (Fe, Cr) sigma phase from austenite, *Acta Metall.* 14 (1996) 1421–1428, [https://doi.org/10.1016/0001-6160\(96\)90162-3](https://doi.org/10.1016/0001-6160(96)90162-3).
- [47] J. Lee, I. Kim, A. Kimura, Application of small punch test to evaluate sigma-phase embrittlement of pressure vessel cladding material, *J. Nucl. Sci. Technol.* 40 (2003) 664–671, <https://doi.org/10.1080/18811248.2003.9715404>.

- [48] T. Sourmail, Precipitation in creep resistant austenitic stainless steels, *Mater. Sci. Technol.* 17 (2001) 1–18, <https://doi.org/10.1179/026708301101508972>.
- [49] H.-H. Lu, H.-K. Guo, W. Liang, The dissolution behavior of  $\sigma$ -phase and the plasticity recovery of precipitation-embrittlement super-ferritic stainless steel, *Mater. Charact.* 190 (2022) 112050, <https://doi.org/10.1016/j.matchar.2022.112050>.
- [50] S. Banerjee, R. Tewari, P. Mukhopadhyay, Coupling of displacive and replacive ordering, *Prog. Mater. Sci.* 42 (1997) 109–123, [https://doi.org/10.1016/s0079-6425\(97\)00010-8](https://doi.org/10.1016/s0079-6425(97)00010-8).